12th International Symposium on Turbulence and Shear Flow Phenomena (TSFP12)
Osaka, Japan (Online), July 19-22, 2022

REGIMES OF NEAR WAKE INTERACTIONS OF A SQUARE BACK BLUFF BODY. CONSEQUENCES FOR DRAG.

Di Bao, Jacques Borée, Yann Haffner* and Christophe Sicot
Institut Pprime
UPR 3346, CNRS-ENSMA-Université de Poitiers
86360 Futuroscope-Chasseneuil, France
Corrsponding address: jacques.boree@ensma.fr
(*)Present address: Centre Scientique et Technique du Bâtiment, Nantes, France

ABSTRACT

The impact of underflow perturbations on the wake and aerodynamic drag of a 3-D square-back bluff body is investigated in order to analyse wheel-vehicle interactions. Two configurations are considered by placing either a pair of D-shaped obstacles or four rotating wheels under the body. For the obstacle configuration, the obstacle width w and the distance from the base to the obstacles l are systematically varied. We reveal two drag-sensitive regimes for $l/w < 2.5$, where the pressure drag of the body is increased up to 22 %. These two regimes present different flow dynamics downstream the obstacles and different scaling properties for the pressure drag. For the wheel configuration with a wheel width w, a similar pressure drag increase is also observed for $l/w < 2.5$. When the wheels were rotated, a scaling for the pressure drag, taking into account the decrease in the wheel wake size, is proposed. In both configurations, the drag increase is associated to a mean mass transfer from the near wake of the body to the wakes of the obstacles or rear wheels.

Introduction

The driving range of ground vehicles at highway speeds is mainly dictated by the aerodynamic drag, which accounts for over 50% of the vehicle's total energy consumption. The dominant contribution to the total pressure drag is the large-scale near wake. The complex interaction between the wheels and this main body wake, however, remains to be understood in detail. This interaction was recently studied in Wang *et al.* (2020) with a basic question: what are the salient features of the flow perturbations induced by wheels that drives this interaction? Starting from rotating/stationary wheels having representative deformable tires, it was shown that the momentum deficit created in the underflow by the wheels, in particular the rear wheels, is an important enabler to this interaction. At first order, it is therefore believed that wheels can be seen as underbody perturbations and that the key aerodynamic features are the underflow blockage, the wheel's wake development in the underflow and its interaction with the near wake of the vehicle.

Even in very simplified reduced scale model studies using reference academic automotive geometries, it is very difficult to achieve a systematic and rigorous survey of the flow mechanisms driving wheel-wake interactions. For example, for obvious mechanical reasons, it is very difficult to change the width of the wheels and their location relative to the base for the same car geometry. Therefore, there is a need for intermediate model configurations that allow a rigorous parametric study using reference underflow perturbations.

Our choice has been to use a Windsor body (e.g. Pavia *et al.* (2020)) and to perturb the wake of this simplified square-back geometry by placing, in the underflow, a pair of streamlined "D-shaped" obstacles of varying width. The two obstacles are mounted at varying relative distances from the base of the body. In a companion experiment, the length of the same body but equipped with rotating wheels and wheelhouses is varied, allowing the relative distance between the rear wheels and the base to be varied. Our goal is first to analyse how the main wake of the body is modified by the wakes of these perturbations, of much smaller size, developing along the underflow. The final goals are to understand how the drag of the body is modified due to the presence of the obstacles and to validate the main findings on the body with wheels and wheelhouses.

Experimental set-up

The experimental setup is shown in figure 1. A square-back Windsor body with height $H = 0.289$ m and width $W = 0.389$ m is placed on a raised floor in the S620 closed-loop wind tunnel at ENSMA with a ground clearance $G = 50$ mm. The blockage ratio over the floor caused by the model is 2.4 %. The length of the body can be modified $L/H = \{3.41, 3.49, 3.59, 3.68, 3.78, 3.87, 3.97\}$. A free-stream velocity $U_0 = 25 ms^{-1}$ is considered, corresponding to a height-based Reynolds number $Re = 4.8 \times 10^5$. The origin O of the coordinate system (x, y, z) is shown in figure $1(a)$.

Two configurations are considered as shown in figure $1(b)$. Firstly, when the wheelhouses of the body with length $L/H = 3.97$ are plugged, a pair of D-shaped obstacles is placed upstream the base of the body, between the underside of the body and the floor. Five values of the width of the obstacles $w/H = \{0.12, 0.16, 0.19, 0.22, 0.26\}$ are tested. The distance from the base of the obstacle to the base of the body is defined as l, which ranges from $l = 0w$ to $l = 5w$. Secondly, when the wheelhouses are not plugged, four electric motors are installed on the floor and are detached from the main body. The rotational speed of the motors Φ, normalized by the speed 3187 RPM matching the free-stream velocity, is varied from 0% to 100%. On each motor, a sharp edge wheel with width $w/H = 0.19$ and diameter $d/H = 0.52$ is installed and is flush to

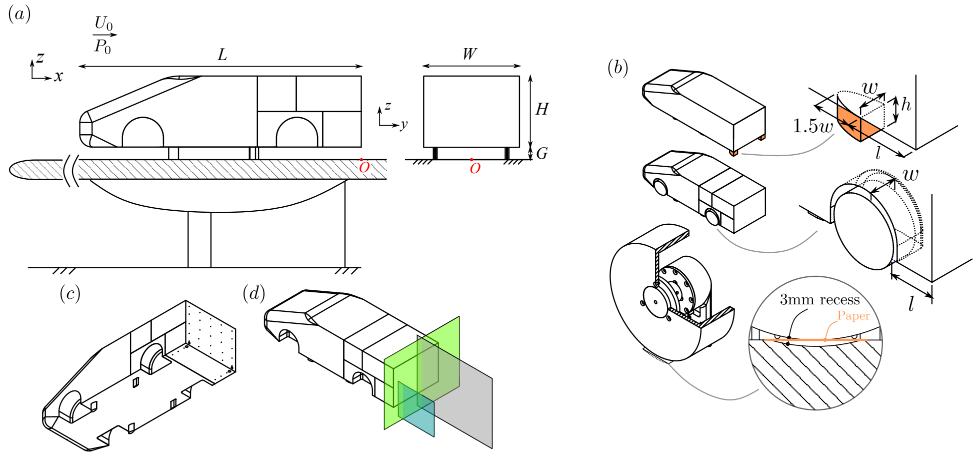

Figure 1. Experimental set-up. (a) Arrangement of the model and the raised floor. (b) Configurations with the use of obstacles and the rotating wheels. (c) Locations of pressure taps on the base and underside of the body. (d) Positions of the particle image velocimetry fields of view.

the floor. A 3 mm deep recess is designed to prevent the contact between the wheel and the floor. However, preliminary tests showed that the resulting gap flow has influence on the base pressure, maximally leading to $\sim 5\%$ base drag decrease. The gap flow is therefore prevented by placing a sealing kraft paper between each wheel and the floor, producing negligible differences in pressure measurements compared to the situation when the recess is fully sealed by high-density foam. The distance from the rear wheels to the base is varied thanks to the variation in the body length, which gives l/w = { 0.65, 1.08, 1.58, 2.08, 2.58, 3.08, 3.58}.

The pressure on the base and underside is monitored by several pressure taps shown in figure $1(c)$ connected to two pressure scanners. Four differential pressure sensors are additionally used for time-resolved measurements. For these sensors, the tubing leads to a cut-off frequency of 150 Hz which is sufficient for resolving the presented time scales. The pressure coefficient $C_p = (p - p_0)/(0.5\rho U_0^2)$ is used to express the pressure measurements, where the reference pressure p_0 is obtained from a pitot tube installed at the ceiling of the test section. The pressure drag of the body is quantified by 25 pressure taps over the base, defined as base drag coefficient: $C_B = -\frac{1}{25}\sum_{i=1}^{25} C_p(y_i, z_i, t)$. The velocity fields in the near-wake are measured by a PIV (Particle image velocimetry) system over three FOVs (fields of view) as depicted in figure $1(d)$. These three FOVs are respectively located at the symmetry plane of the model (y/H = 0), the symmetry plane of the left-hand wheels (y/H = -0.58) and a cross-flow plane in proximity to the base (x/H = 0.03). Two-component (2D2C) and stereoscopic (2D3C) PIV set-ups are respectively used for the first two FOVs and the last FOV.

Results and discussion

The flow over the basic Windsor body was first carefully measured. A detailed description for the basic body with length $L/H = 3.97$ can be found in Bao *et al.* (2022). Briefly, the large-scale near wake presents a vertical well-balanced mean topology with horizontal bi-stable dynamics (Grandemange *et al.*, 2013). There is a slight base drag increase from $\overline{C_{B0}} = 0.189$ to 0.198 with decreasing body length from $L/H = 3.97$ to 3.41, possibly due to the modifications in the boundary layer profile at separation (Mariotti *et al.*, 2015). However no obvious changes in the wake properties are observed. For the longest body with underflow perturbed by the obstacle pair, the variation of the base drag $\Delta\overline{C_B} = \overline{C_B} - \overline{C_{B0}}$ for different obstacle widths w/H with varying obstacle-to-base distance l/w is presented in figure $2(a)$. Here the relative distance l/w is the relevant scaling as the distance to the base is concerned. Based on the mean and fluctuating properties measured downstream the obstacles (discussed later), two successive drag-sensitive regimes are identified for obstacle-to-base distances $l/w < 2.5$, where pressure drag of the body is increased up to 22%. In different regimes, different scaling properties for the base drag are observed (see figure 5 in Bao *et al.* (2022) for the scalings). In regime I, the base drag increase from the plateau ($l/w > 2.5$) scales quadratically with w. In regime II, the base drag increase relative to the unperturbed case scales linearly with w.

The base drag sensitivity observed using obstacles is also witnessed in the more applied situation when the wheels and wheelhouses are installed. The base drag evolution relative to the unperturbed cases $\overline{C_B}(l/w)/\overline{C_{B0}}(l/w)$ for different rotational speed Φ is presented in figure $2(b)$. The obstacle configuration with the same $w/H = 0.19$ as the wheel is also shown for comparison. With decreasing l/w, the base drag presents first a plateau with a slight increase in base drag, followed by a rapid base drag increase, maximally leading to a base drag increase of $\sim 13\%$ for $l/w = 0.65$. The trend of base drag increase is very similar to regime I of the obstacle configuration. Moreover, we also notice a slight decrease in base drag with the increase in the rotational speed Φ. Considering that the wake of rotating wheels is shorter and narrower compared to stationary ones (Wäschle, 2007; Wang *et al.*, 2020), an empirical scaling for the base drag, validated later by local pressure and velocity measurements, is simply obtained by defining an equivalent width $w^* = w/(1+0.2\Phi)$. Figure $2(b)$ shows a collapse of all data on a single evolution when l/w^* is used.

Local pressure measurements are now investigated in order to reveal the location of base drag increase. The base pressure distributions $\langle\overline{C_p}\rangle$ ($\langle\rangle$ denotes space-averaging from the left-hand and the right-hand sides) and their changes relative to the unperturbed cases $\Delta\langle\overline{C_p}\rangle$ are shown in figure $3(a)$. The selected representative cases are the wheel cases with maximum and minimum l/w and the $w/H = 0.19$ obstacle cases of the plateau and the two regimes. We first focus on the obstacle configuration. In the plateau, the base pressure decrease of $\sim 5\%$ from the unperturbed case is located at the bottom half

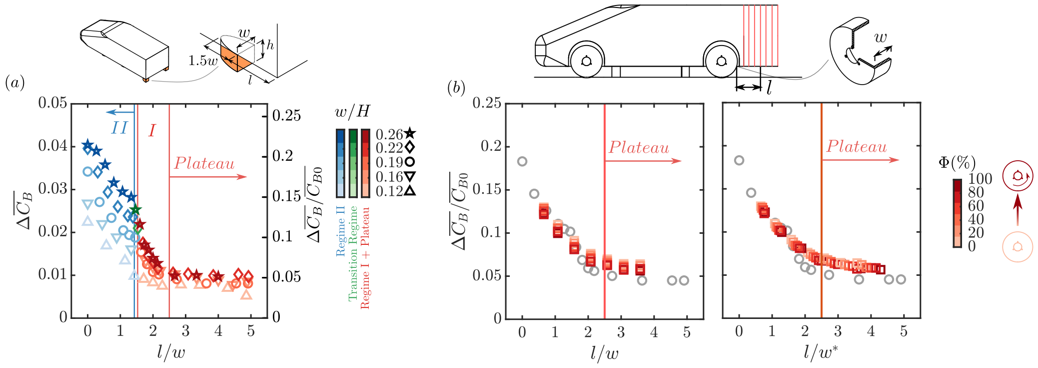

Figure 2. (a) Impact of the position l and width w of the obstacles on the base drag of the body, darker color indicates wider obstacle, different colors indicate different flow regimes (see text). (b) Base drag of the body $\Delta\overline{C_B}/\overline{C_{B0}}$ as a function of the distance from the base to the rear wheel l, darker color indicates higher rotational speed Φ, l is scaled with the width of the wheel w and a reduced width depending on the rotating speed $w^* = w/(1+0.2\Phi)$.

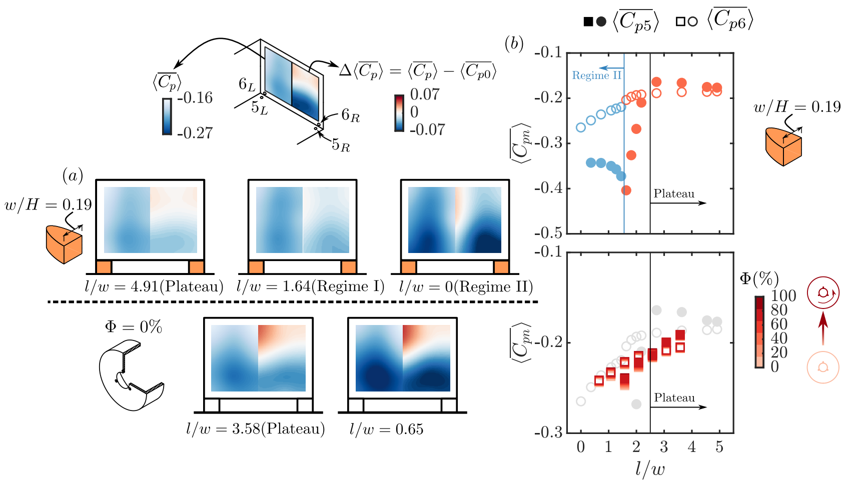

Figure 3. (a) Evolution of the base pressure distribution with the distance from the base to the obstacles or to the rear wheels l/w, the mean values and the differences with respect to the unperturbed case are respectively presented at the left and right sides of the base. (b) Comparison between the evolution of $\langle\overline{C_{p5}}\rangle$ and $\langle\overline{C_{p6}}\rangle$. The width of the obstacle pair is $w/H = 0.19$.

of the base with a slight pressure recovery at the top half. In regime I, we observe a further pressure decrease at the bottom half of the base with now also a slight decrease at the top half. The pressure decrease is not homogeneous laterally but rather located near the obstacles. In regime II, the base pressure is importantly modified and the modification is mainly located at the bottom half of the base and horizontally near the obstacle pair. Indeed, both regimes share the same feature with pressure drop near the obstacle pair. This feature is also observed for the wheel configuration.

In order to study the relation between local near wake interactions and base pressure variation, we consider the pressure distribution in the vicinity of the obstacles or the rear wheels. In figure 3(b) a comparison is presented between the evolution of $\langle\overline{C_{p5}}\rangle$ and $\langle\overline{C_{p6}}\rangle$ for the reference configuration. As shown in the sketch, pressure sensors numbered 5 and 6 are situated in the symmetry plane of the rear wheels or obstacles and are located at both sides of the bottom trailing edge. These are the key locations for the problem considered here. For the obstacle configuration, in the plateau, $\langle\overline{C_{p5}}\rangle$ is slightly higher than $\langle\overline{C_{p6}}\rangle$. This is expected for a mean curved streamline after separation, inducing a lower pressure inside the recirculating bubble due to centrifugal effect. However in both regime I and II, $\langle\overline{C_{p5}}\rangle$ is lower than $\langle\overline{C_{p6}}\rangle$. With decreasing l/w, the pressure difference $\langle\overline{C_{p6}}\rangle - \langle\overline{C_{p5}}\rangle$ increases strongly in regime I. On the contrary, in regime II, $\langle\overline{C_{p6}}\rangle - \langle\overline{C_{p5}}\rangle$ decreases with decreasing l/w. For the wheel configuration, the same observation as the regime I of the obstacle configuration is achieved.

The influence of the obstacles on the main wake as presented using $\langle\overline{C_{p5}}\rangle$ changes rapidly in the drag-sensitive regimes. The streamwise pressure development downstream the obstacles or the wheels is therefore investigated. The pressure coefficients obtained from the available pressure taps behind the obstacles/wheels are used. Each pressure measurement is plotted against the relative distance x_w/w from the tap to the base of the obstacle or the most downstream position of the rear wheels (detailed in figure 7 of Bao *et al.* (2022)). For the obstacle configuration (figure 4(a)), a nice collapse is found for all the cases with two different streamwise pressure developments of the obstacle wake in two regimes - green symbols corresponds to transition between regimes. In regime I (colored in red), the development is similar to the measurements for 2-D D-shaped bluff bodies (Bearman, 1967; Park *et al.*, 2006) with comparable pressure level near the base. The sharp pressure change in $1 < x_w/w < 2$ can be linked to the vortex shedding motion of the obstacle through a streamwise momentum balance along the centerline of the obstacle as shown in Bao *et al.* (2022). In regime II (colored in blue), the pressure near the obstacle base shows a higher level than regime I, indicating that the obstacle wake is completely mod-

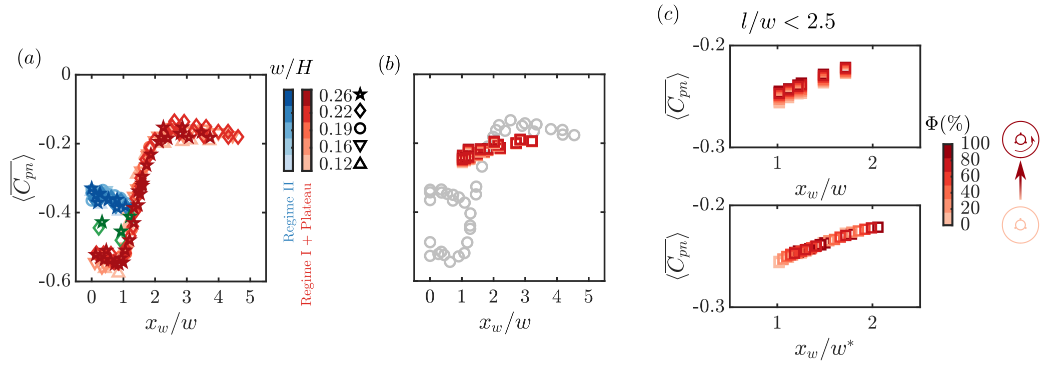

Figure 4. Pressure evolution in the wakes of the obstacles (a) and of the rear wheels (b). x_w/w is the relative distance from the base of the obstacle or from the most downstream location of the rear wheel. For the cases of the wheel configuration with $l/w < 2.5$, the relative distance x_w/w is either scaled with the wheel width w or the reduced width w^* in (c) (see also fig. 7 of Bao *et al.* (2022)).

ified by the near wake interactions. For the wheel configuration (figure 4(b)), a similar pressure decrease as regime I with x_w/w is also measured but the slope is smaller than the obstacle. For the cases in the drag-sensitive regime $l/w < 2.5$ as shown in figure 4(c), the reduced width w^* is able to collapse the pressure developments of different cases involving different rotational speeds Φ and different l/w.

We now investigate the pressure dynamics in the wake of the obstacles or the wheels. The coherent dynamics of the obstacle wake are captured by taps 5_L and 5_R located downstream of the obstacles or the wheels. The premultiplied spectra obtained from 5_L and 5_R are averaged and are shown in figure 5(a). For the obstacle configuration, a clear distinction is noticed between the cases, where an important peak is noticed for the case in regime I. This peak occurs at $St_w = 0.26$ which is in good agreement with the studies based on D-shaped cylinders (Bearman, 1967; Park *et al.*, 2006). In these studies, the authors interpret the peak frequency as the vortex shedding frequency. On the other hand in regime II, the peak at $St_w = 0.26$ is barely discernible, implying suppression of the periodic motion. For the wheel configuration, we notice a peak at $St_w = 0.15$. Interestingly, Croner *et al.* (2013) experimentally measured a dominant peak at $St_w = 0.14$ downstream an isolated wheel using a hotwire probe, numerically it matches the fluctuation of the side force coefficient. Therefore in our case, the peak at $St_w = 0.15$ may represent horizontal coherent motion of the wheel wake, in the same direction as the horizontal vortex shedding of the obstacles in regime I. The dynamics of the obstacle or wheel wake has influence on the base pressure dynamics. This is shown in figure 5(b) by the premultiplied spectra obtained from 6_L and 6_R. For the wheel configuration, the dominant peak is observed down to $l/w = 0.65$ while a sharp change at $l/w = 1.56$ is observed for the 2-D obstacle pair.

Now the velocity fields are examined to reveal the flow mechanisms responsible for the base drag increase, starting from the mean topology of the main body wake in the symmetry plane as shown in figure 6. We notice a vertical asymmetry for the wheel configuration, possibly related to the presence of the front wheels that reduce the underbody flow rate. The reduction in l/w brings slight changes in the topology as indicated by the recirculation length (not discussed here for brevity), defined as $L_r = max(x/H)_{\overline{u_x}(x/H)\leq 0}$. A more pronounced change is observed in the strength of recirculation, quantified by: $\mathscr{R}(x) = \int_{\overline{u_x}\leq 0} |\overline{u_{xz}}(x,z)| dz$, where $|\overline{u_{xz}}| = \sqrt{\overline{u_x}^2 + \overline{u_z}^2}$. For both configurations, we notice a substantial increase in $\mathscr{R}$ with decreasing l/w.

The investigation is then focused on the stereo PIV measurements in the cross-flow plane at $x/H = 0.03$ (figure 7). For the obstacle configuration, in the plateau, the main wake is bounded by shear layers. With decreasing l/w, an important momentum deficit is observed behind the obstacles in regime II, followed by a wake merging in regime I. This is better illustrated by plotting the streamwise velocity along the symmetry line of the left-hand obstacle in figure 7(b). We notice first a gradual reduction of shear between the wake of the body and the wake of the obstacle from the plateau to regime I. Then the wakes are merged in regime II, with $\overline{u_x} < 0$ in the region downstream the obstacle. For the wheel configuration, the shear is substantially reduced from the maximum l/w case to the minimum l/w case. However, no recirculating flow is captured in the velocity field downstream the wheels.

A mean mass transfer from the main wake to the wakes of the obstacles is observed in figure 7(a) by considering the in-plane vector fields. The strength of the mass flux is quantified by space-averaging the mean vertical velocity in the present plane over the width w at the interface between the main body and the obstacle, which is shown in figure 7(c). In regime II the mass flux has a velocity of approximately 20 % of the free-stream velocity. This is also observed – with lower intensity – in regime I as well as for the minimum l/w case of the wheel configuration.

The aforementioned velocity measurements only focus on the stationary wheel cases. Indeed, for those measurements, only slight differences are noticed between the stationary cases and the corresponding rotating cases. However, the streamwise velocity developments measured in the symmetry plane downstream of stationary and rotating wheels are very different as shown in figure 8. In accordance with Wang *et al.* (2020), the wake of the rotating wheel is shorter than that of the stationary wheel. This is clearly shown in figure 8(b) by plotting the streamwise velocity $\overline{u_x}$ evolution along the height of the ground clearance G against the distance to the base of the body x/H. A higher $\overline{u_x}$ is measured near the base for the rotating case than for the stationary case. We then plot $\overline{u_x}$ against the distance from the most downstream location of the wheel x_w, which scales with the reduced width w^*. This shows a nice collapse in the interaction region $x_w/w^* < 3$. Moreover, the mass transfer from the main wake to the wakes of the wheels is also measured in this plane by the vertical velocity component $\overline{u_z}$. The streamwise development along the ground clearance line is plotted in a similar fashion as the $\overline{u_x}$ evolution. The reduced width w^* collapses the region with negative $\overline{u_z}$.

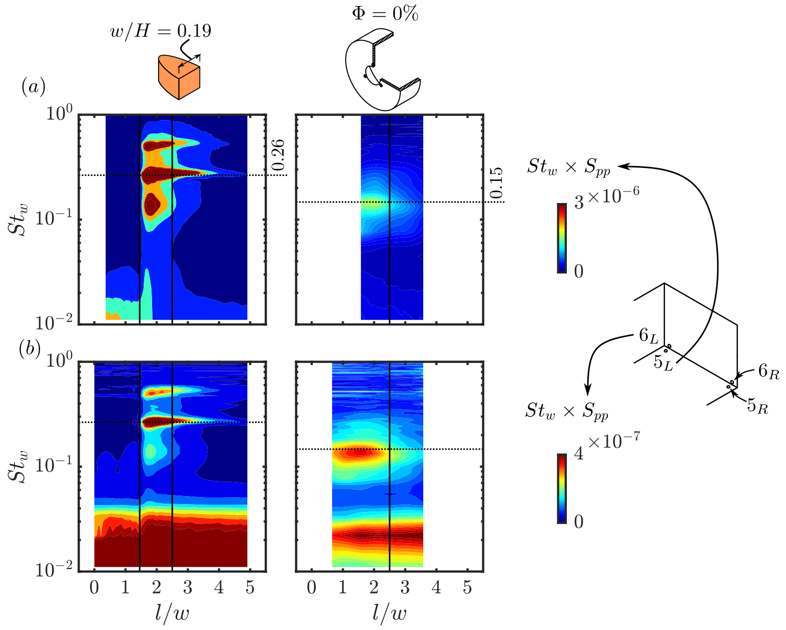

Figure 5. Evolution of the premultiplied spectrum of the pressure signal C_{p5} (a) and C_{p6} (b) with the obstacle-to-base or wheel-to-base distance l/w.

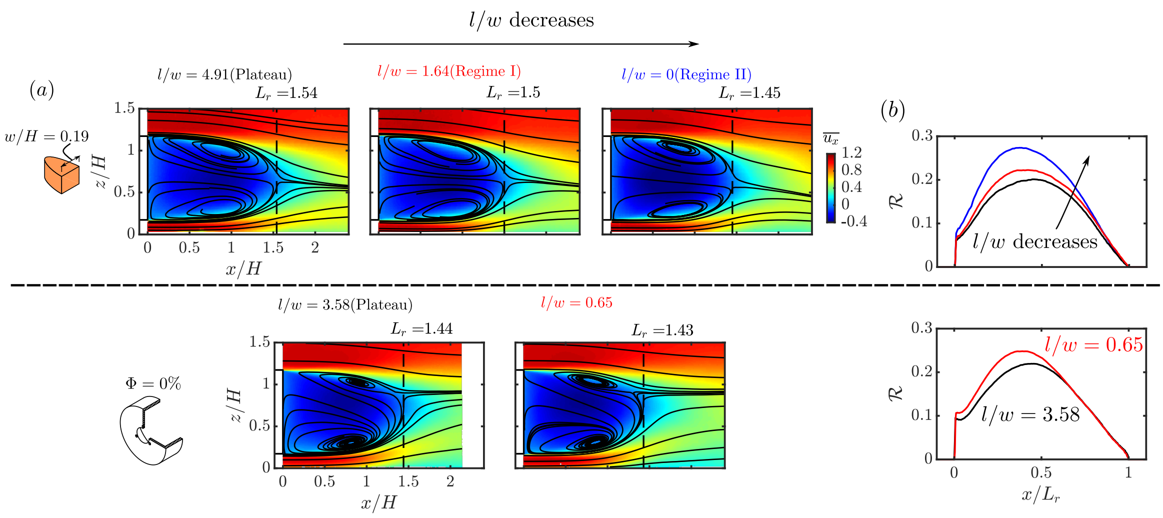

Figure 6. (a) Evolution of the main wake topology with the obstacle-to-base distance or wheel-to-base distance l/w. (b) Comparison of the recirculation strength $\mathscr{R}$ for the cases presented in (a).

Conclusion

The impact of underflow perturbations on the wake and aerodynamic drag of a 3-D square-back bluff body was investigated in order to analyse wheel-vehicle interactions. Two configurations were considered by placing either a pair of D-shaped obstacles or four rotating wheels under the body. For the obstacle configuration, the obstacle width w and the distance from the base to the obstacles l were systematically varied. We revealed two drag-sensitive regimes for $l/w < 2.5$. These two regimes present different flow dynamics downstream the obstacles and different scaling properties for the pressure drag. For the wheel configuration with a wheel width w, a similar pressure drag increase is also observed for $l/w < 2.5$. When the wheels were rotated, a scaling for the pressure drag, taking into account the decrease in the wheel wake size, was proposed.

Despite these important differences between either the two regimes or the shapes of the perturbations, a mean mass transfer is always observed from the near wake of the body to the wakes of the obstacles or rear wheels. Using our results and the reference studies (Bearman, 1967; Hsu *et al.*, 2021) describing the effect of base suction on the pressure drag of bluff bodies, a physical model based on a flow momentum balance of the wake is proposed in Bao *et al.* (2022) to explain the scalings in different configurations. For the first regime ($l/w < 1.5$) of the obstacle configuration, the pressure drag scales with w. This implies that the size of the mass exchange surface is governed by both the scale of the obstacle and the scale of the body. On the other hand, For the second regime ($1.5 < l/w < 2.5$), a w^2 scaling is found which can be simply understood by stating that both the width and length of the surface of the mass exchange are driven by the size of the obstacle w. For the obstacle configuration, the scaling points to a decrease in the length of the exchange surface with increasing rotational speed. Our experimental data are all in agreement with this model.

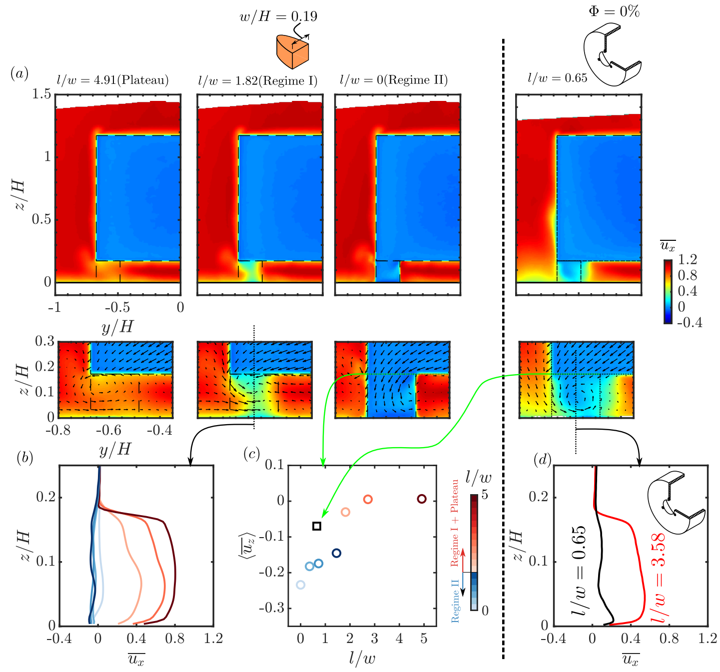

Figure 7. (a) Evolution of the mean streamwise velocity $\overline{u_x}$ with the obstacle-to-base or wheel-to-base distance l/w at $x/H = 0.03$ near the base of the body. The velocity distributions along the symmetry line of the left-hand obstacle/wheel are presented in (b)/(d). The space-averaged vertical velocity $\langle \overline{u_x} \rangle$ along the line indicated is plotted against l/w in (c).

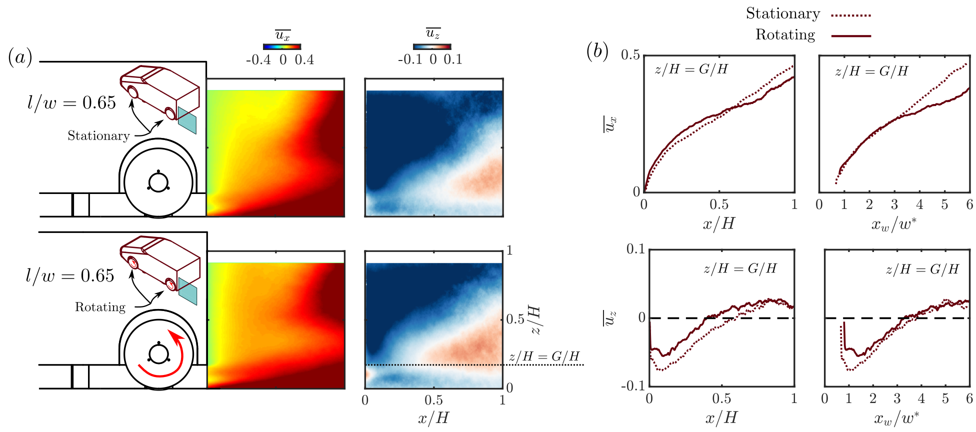

Figure 8. (a) Velocity distributions in the symmetry plane of the left wheels ($y/H = -0.58$) for the stationary and full rotating cases ($\Phi = 100\%$), the wheel-to-base distance is $l/w = 0.65$. The streamwise velocity $\overline{u_x}$ and the vertical velocity $\overline{u_z}$ along the ground clearance line are plotted in (b) with different scalings.

REFERENCES

Bao, D., Borée, J., Haffner, Y. & Sicot, C. 2022 Near wake interactions and drag increase regimes for a square-back bluff body. *J. Fluid Mech.* **936**.

Bearman, P.W. 1967 The effect of base bleed on the flow behind a two-dimensional model with a blunt trailing edge. *Aeronaut. Q.* **18** (3), 207–224.

Croner, E., Bézard, H., Sicot, C. & Mothay, G. 2013 Aerodynamic characterization of the wake of an isolated rolling wheel. *Int. J. Heat Fluid Flow* **43**, 233–243.

Grandemange, M., Gohlke, M. & Cadot, O. 2013 Turbulent wake past a three-dimensional blunt body. part 1. global modes and bi-stability. *J. Fluid Mech.* **722**, 51.

Hsu, E.C., Pastur, L., Cadot, O. & Parezanović, V. 2021 A fundamental link between steady asymmetry and separation length in the wake of a 3-d square-back body. *Exp. Fluids* **62** (5).

Mariotti, A., Buresti, G. & Salvetti, M. V. 2015 Connection between base drag, separating boundary layer characteristics and wake mean recirculation length of an axisymmetric blunt-based body. *J. Fluids Struct* **55**, 191–203.

Park, H., Lee, D., Jeon, W., Hahn, S., Kim, J., Kim, J., Choi, J. & Choi, H. 2006 Drag reduction in flow over a two-dimensional bluff body with a blunt trailing edge using a new passive device. *J. Fluid Mech.* **563**, 389.

Pavia, G., Passmore, M.A., Varney, M. & Hodgson, G. 2020 Salient three-dimensional features of the turbulent wake of a simplified square-back vehicle. *J. Fluid Mech.* **888**, A33.

Wang, Y., Sicot, C., Borée, J. & Grandemange, M. 2020 Experimental study of wheel-vehicle aerodynamic interactions. *J. Wind Eng. Ind. Aerodyn.* **198**, 104062.

Wäschle, A. 2007 The influence of rotating wheels on vehicle aerodynamics-numerical and experimental investigations. *Tech. Rep.* 2007-01-0107. SAE, Inc.